

NUMERICAL SOLUTION OF HYDROMAGNETIC PERISTALTIC FLOW IN A POROUS-SATURATED HEATED CHANNEL

by

Raheel AHMED* and Nasir ALI

Department of Mathematics and Statistics,
International Islamic University, Islamabad, Pakistan

Original scientific paper
<https://doi.org/10.2298/TSCI170825006A>

The hydromagnetic-flow in sinusoidally heated porous channel is studied by utilizing Darcy-Forchiemmer law with Joule heating effect. The Darcy's resistance term in the momentum equation is acquired by using modified Darcy's law. The governing equations for flow velocity, temperature, and mass concentration are developed under lubrication approximation, commonly known as long wavelength assumption in the realm of peristaltic flows. A well-tested implicit finite difference scheme is employed to solve the set of these equations along with appropriate boundary conditions. The governing equations involve important parameters namely, Forchiemmer parameter, dimensionless radius of curvature, permeability parameter, Hartmann, Brinkmann, Schmidt, and Soret numbers. The effect of these important parameters on velocity, temperature and mass concentration is illustrated through graphs. The pressure-flow rate relationship and streamlines are also shown. The presence of porous matrix inside the channel impedes the flow velocity and reduces the peristaltic transport and mingling. Moreover, temperature of the fluid rises with decreasing permeability of porous-matrix and Hartmann number.

Key-words: *Joule heating, hydromagnetic, porous media, Reynolds number, Darcy law*

Introduction

In fluid dynamics, the flow due to sinusoidal motion of the vessel walls is known as peristaltic flow. The rhythmic contractions and relaxations of smooth muscles of the vessel produce peristaltic motion. Peristaltic flows are found in numerous physiological and industrial processes. The food in digestive system, urine from kidneys to the bladder, chyme in small intestine and blood in small blood vessels are transported in human body according to peristaltic mechanism. Industrial applications of peristalsis can be found in diabetic pumps, heart-lung machine, roller and finger pumps, *etc.* Several theoretical and experimental studies have been carried out in past to investigate the fluid dynamics of this mechanism.

The first comprehensive study of peristaltic transport was carried out by Shapiro *et al.* [1] under long wavelength and low Reynolds number assumptions in wave frame of reference. They modeled the flow in both channel and axisymmetric tube using Navier-Stokes equations. Fung and Yih [2] dropped the assumptions of long wavelength and low Reynolds number and analyzed the peristaltic flow in fixed frame of reference. The approach of Shapiro *et al.* [1] was extended by several authors to include non-Newtonian effects [3-7], slip effects [8-10]

* Corresponding author, e-mail: raheel_rwp@yahoo.com

and electro-osmotic effects [11]. The important phenomena of heat and mass transfer have also been investigated in peristaltic flows by several authors with a motivation of its applications in hemodialysis, laser therapy and cryosurgery. Moreover, in various peristaltic pumps, heat transfer phenomena plays a vital role and is strongly affected by the peristaltic flow field. The interaction of heat transfer and peristaltic flow of Newtonian and non-Newtonian fluids has been reported in different geometrical set-ups. For instance, Vajravelu *et al.* [12] studied heat transfer in peristaltic flow through a porous vertical annulus. Mekheimer and Abd Elmaboud [13] discussed the heat transfer on peristaltic flow in a vertical annulus under long wavelength and low Reynolds number approximations. Ali *et al.* [14] analyzed the curvature effects on heat transfer for peristaltic flow of Newtonian fluid in a curved channel. Tripathi *et al.*, [15] presented the mathematical model to describe the effects of heat transfer on dynamics of food bolus through the esophagus. When heat and mass transfer occur simultaneously in a moving fluid, then it affect many transport processes present in nature and also the applications relating to science and engineering. In processes such as the flow in a desert cooler, energy transfer in a cooling tower, evaporation, and drying, heat and mass transfer occur simultaneously. Eldabe *et al.* [16] has studied the problem of peristaltic transport of a non-Newtonian fluid with variable viscosity in the presence of heat and mass transfer between vertical walls. Srinivas and Kothandapani [17] examined the effects of heat and mass transfer on peristaltic transport in a porous space with compliant walls. Hayat *et al.* [18] studied the effect of wall properties on peristaltically driven flow of third grade fluid in a curved channel with heat and mass transfer. Srinivas *et al.* [19] observed the effect of mixed convective heat and mass transfer on peristaltic flow in an asymmetric channel.

Recently, Ahmed *et al.* [20] investigated the effects of heat and mass transfer on the peristaltic flow of Sisko fluid in a curved channel. The aforementioned attempts regarding heat/mass transfer in peristaltic flow are also based on the approach of Shapiro *et al.* [1]. On other hand, the analysis of Fung and Yih [2] is only generalized to include compressibility effects [21-26].

Porous medium is a stuff that contains spaces between solid areas through which fluid can pass. The flow of fluid through a porous media is a subject of most common interest and has emerged as separate field in the realm of fluid-flows. In the recent years considerable interest has been noticed to the study of viscous flows through porous media because of its natural occurrence and its importance in industrial geophysical and medical applications. Some practical problems involving such studies include the extraction and filtration of oil from wells, the drainage of water for irrigation, the percolation of water through solids and the seepage through slurries in drains by the sanitary engineer, the flow of oils through porous rocks, the extraction of energy from geo-thermal regions, the flow of liquids through ion-exchange beds, cleaning of oil-spills, *etc.*, are some of the areas in which flows through porous media are noticed. The flow through the porous media is usually studied utilizing Darcy's law which linearly relates flow velocity and pressure gradient through the porous medium. Permeability of the porous medium is an important parameter in the Darcy's relation. Two important extension of Darcy law can also be found in the literature, namely, Darcy-Forchiemmer law and Darcy-Forchiemmer extended law which non-linearly relate the flow velocity and pressure drop. The foremost contribution on flows through porous media was made by Brinkman [27], who calculated the viscous force exerted by a flowing fluid through a porous media. Peristaltic flows through porous medium is also an active area of research. Several authors contributed to this area. Mention may be made to the work of El Shehawey [28], Mekheimer [29], Kothandapani *et al.* [30], and Hayat *et al.* [31] in various scenarios.

The MHD is the study of dynamics of conducting fluids in the presence of an applied magnetic field. Examples of MHD fluids are plasma, blood, liquid metals, and salt or sea water. The equations describing MHD fluids are the combination of Navier-Stokes equations and Maxwell equations of electromagnetism. Wang *et al.* [32] thoroughly studied the effects of magnetic field on peristaltic flow of Sisko fluid in symmetric or asymmetric channel. Hayat and Hina [33] described the influence of wall properties on the MHD peristaltic flow of a Maxwell fluid with heat and mass transfer. Tripathi and Beg [34] examined various features of MHD flow through a finite length channel by peristaltic pumping. Reddy [35] investigated the effects of magnetic field and porous medium in peristaltic slip flow with heat and mass transfer. The effect of homogenous/ heterogeneous reaction and thermal slip in non-isothermal MHD flow of third order in an irregular porous-saturated channel are also discussed by Reddy [36]. Reddy and Makinde [37] investigated MHD peristaltic flow of Jeffrey nanofluid in an asymmetric inclined channel. Heat transfer analysis in rotating MHD peristaltic flow of Jeffrey fluid in an asymmetric channel is carried out by Reddy *et al.* [38]. Peristaltic motion of reacting and rotating couple stress fluid in inclined asymmetric channel is also studied by Reddy *et al.* [39]. Carreau and Casson models are integrated by Reddy *et al.* [40] to describe the effects of nanoparticles in hydromagnetic radiative peristaltic flow in an irregular channel. More recently, Makinde *et al.* [41] discussed the radiation effects on hydromagnetic-flow of Walter-B fluid in presence of heat source and slip conditions.

Joule heating appears due to the resistance offered to electric current while passing through some material. There are number of systems in which Joule heating effect has vital role such as dielectrophoretic trapping, electric fuses, PCR reactors, hot plate, microvalves for fluid control, electric heaters and stoves, thermistors and soldering irons, *etc.* On the other hand in some mechanism it generates undesired heat which can degenerate or melt the machinery parts, may create denaturation of biological samples like DNA, flopping of chip systems and bubble formation, *etc.* Such undesired effects of Joule heating can be controlled to some extent. A number of studies describe the joule heating effect on peristalsis. For detail see [42-44].

In all the cited literature, the peristaltic flow is modeled for planar channel, axisymmetric tube, curved channel or a rectangular duct. Moreover the studies pertaining to peristaltic flow in curved channel are limited to flow and heat transfer analysis. Less attention is focused to analyze the flow and heat/ mass transfer characteristics in porous-saturated curved channel with Joule heating effect. With aforementioned facts in mind, the aim of this article is to model the problem of flow and heat/mass transfer in a curved channel in presence of porous media and Joule heating effects. The system of equations is developed for the case when wave number is vanishingly small. A well-tested finite difference scheme is employed for the solution. Impact of pertinent parameters on physical quantities of interest are discussed in detail.

Mathematical formulation

Consider a curved channel of width $2w$ coiled in a circle having radius R_0 and center O . A homogenous fluid-flows inside the porous-saturated channel due to the sinusoidal deformation of the channel walls. The flow is also subjected to an applied magnetic field in the radial direction. Let c be the speed of the waves propagating along the channel walls while a and b denote the amplitudes of the upper and lower walls of the channel, respectively. The upper and lower walls of the channel are maintained at constant temperature T_0 and T_1 , respectively. Similarly, C_0 and C_1 specify the mass concentration at upper and lower walls, respectively. The flow can be well described in a curvilinear co-ordinate system (R, χ, Z) , in which R is oriented along

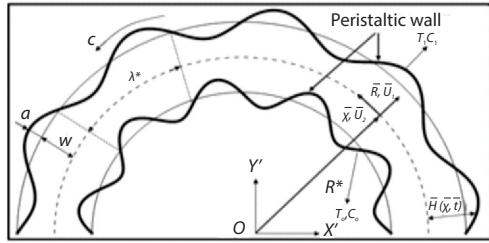


Figure 1. Physical sketch of peristaltic flow regime

radial direction, χ is along the flow direction, and Z is perpendicular to the plane spanned by R and χ . The geometry and co-ordinate system are illustrated in fig. 1. The shape of both walls is described mathematically:

– upper wall

$$H_1(\chi, t) = w + a \sin \left[\left(\frac{2\pi}{\lambda^*} \right) (\chi - ct) \right] \quad (1)$$

– lower wall

$$H_2(\chi, t) = -w - b \sin \left[\left(\frac{2\pi}{\lambda^*} \right) (\chi - ct) \right] \quad (2)$$

where λ^* is the wavelength and t – the time.

It is intended to determine the flow, temperature and concentration fields. Due to complex nature of transport process in porous medium, the present work is based on simplified mathematical model with the following assumptions:

- The medium is homogenous and solid material does not chemically interact with the permeating fluid.
- The medium is isotropic.
- The fluid is assumed as a continuum.
- The fluid is single phase and obeys classical Newtonian constitutive equation. The density of fluid is constant *i. e.*, fluid is incompressible.
- No heat source or sink exist in the channel. Moreover, thermal radiation effects are negligible.
- The solid matrix is in a local thermal equilibrium with the fluid.
- The walls of the channel are non-compliant.
- Flow is laminar with negligible gravitational effects.
- Magnetic Reynolds number is assumed small and hence effects of induced magnetic field are negligible.
- Joule heating and Soret effects are taken into account.

In view of previous assumptions the equations governing the flow, heat, and mass transfer:

– continuity equation

$$\nabla \cdot \mathbf{U} = 0 \quad (3)$$

– momentum equation

$$\rho \frac{d\mathbf{U}}{dt} = \nabla \cdot \boldsymbol{\tau} - \frac{\mu}{k^*} \mathbf{U} - \frac{\rho CE}{\sqrt{k^*}} |\mathbf{U}| \mathbf{U} + \mathbf{J} \times \mathbf{B} \quad (4)$$

– energy equation

$$\rho c_p \frac{dT}{dt} = k \nabla^2 T + \mu \Phi + \frac{\sigma B_0^2 \tilde{R}^2}{(R + \tilde{R})^2} U^2 \quad (5)$$

– mass concentration equation

$$\frac{dC}{dt} = D \nabla^2 C + \frac{DK_T}{T_m} \nabla^2 T \quad (6)$$

where \mathbf{U} is the velocity, τ – the Cauchy stress tensor, T – the temperature, CE – the dimensionless form-drag constant, C – the mass concentration, c_p – the specific heat at constant pressure, k^* – the permeability of porous medium, μ – the viscosity of porous medium, k – the thermal conductivity (assumed constant), D – the coefficient of mass diffusivity, K_T – the thermal diffusivity, T_m – is the mean temperature, Φ – the dissipation function, σ – the Stefan-Boltzman constant, and ρ – the fluid density. The form of the radial magnetic field \mathbf{B} :

$$\mathbf{B} = \left(\frac{B^* \tilde{R}}{R + \tilde{R}} \right) \mathbf{e}_R \tag{7}$$

where B^* is the characteristic magnetic induction in the limit $\tilde{R} \rightarrow \infty$ and \mathbf{e}_R – the unit vector in the radial direction. It is pointed out here that the magnetic field given by eq. (7) is solenoidal and satisfies Maxwell’s equations.

Using eq. (7), the term $\mathbf{J} \times \mathbf{B}$ in eq. (4) is given [7]:

$$\mathbf{J} \cdot \mathbf{B} = - \left[\frac{\sigma B^{*2} U_2 \tilde{R}^2}{(R + \tilde{R})^2} \right] \mathbf{e}_\chi \tag{8}$$

where \mathbf{e}_χ is the unit vector in the azimuthal direction.

Assuming:

$$\mathbf{U} = [U_1(\chi, R, t), U_2(\chi, R, t), 0], T = T(\chi, R, t), C = C(\chi, R, t)$$

Equations (3)-(6) yield:

$$\frac{\partial}{\partial R} [(R + \tilde{R})U_1] + \tilde{R} \frac{\partial U_2}{\partial \chi} = 0 \tag{9}$$

$$\begin{aligned} & \frac{\partial U_1}{\partial t} + U_1 \frac{\partial U_1}{\partial R} + \frac{RU_2}{R + \tilde{R}} \frac{\partial U_1}{\partial \chi} - \frac{U_2^2}{R + \tilde{R}} = - \frac{1}{\rho} \frac{\partial P}{\partial R} + \\ & + \nu \left[\frac{1}{R + \tilde{R}} \frac{\partial}{\partial R} \left\{ (R + \tilde{R}) \frac{\partial U_1}{\partial R} \right\} + \left(\frac{\tilde{R}}{R + \tilde{R}} \right)^2 \frac{\partial^2 U_1}{\partial \chi^2} - \frac{U_1}{(R + \tilde{R})^2} - \frac{2\tilde{R}}{(R + \tilde{R})^2} \frac{\partial U_2}{\partial \chi} \right] - \\ & - \frac{\mu}{\rho k^*} U_1 - \frac{CE}{\sqrt{k^*}} U_1^2 \end{aligned} \tag{10}$$

$$\begin{aligned} & \frac{\partial U_2}{\partial t} + U_1 \frac{\partial U_2}{\partial R} + \frac{\tilde{R}U_2}{R + \tilde{R}} \frac{\partial U_2}{\partial \chi} + \frac{U_2 U_1}{R + \tilde{R}} = - \frac{\tilde{R}}{\rho(R + \tilde{R})} \frac{\partial P}{\partial \chi} + \\ & + \nu \left[\frac{1}{(R + \tilde{R})} \frac{\partial}{\partial R} \left\{ (R + \tilde{R}) \frac{\partial U_2}{\partial R} \right\} + \left(\frac{\tilde{R}}{R + \tilde{R}} \right)^2 \frac{\partial^2 U_2}{\partial \chi^2} - \frac{U_2}{(R + \tilde{R})^2} + \frac{2\tilde{R}}{(R + \tilde{R})^2} \frac{\partial U_1}{\partial \chi} \right] - \\ & - \frac{\mu}{\rho k^*} U_2 - \frac{CE}{\sqrt{k^*}} U_2^2 - \frac{\sigma B^{*2} U_2 \tilde{R}^2}{(R + \tilde{R})^2} \end{aligned} \tag{11}$$

$$\rho c_p \left[\frac{\partial T}{\partial t} + U_1 \frac{\partial T}{\partial R} + \frac{\tilde{R} U_2}{R + \tilde{R}} \frac{\partial T}{\partial \chi} \right] = k \left\{ \frac{1}{(R + \tilde{R})} \frac{\partial}{\partial R} \left[(R + \tilde{R}) \frac{\partial T}{\partial R} \right] + \left(\frac{\tilde{R}}{R + \tilde{R}} \right)^2 \frac{\partial^2 T}{\partial \chi^2} \right\} +$$

$$+ \mu \left[2 \left(\frac{\partial U_1}{\partial R} \right)^2 + \left(\frac{\tilde{R}}{R + \tilde{R}} \frac{\partial U_1}{\partial \chi} - \frac{U_2}{R + \tilde{R}} \right) \left(\frac{\partial U_2}{\partial R} + \frac{\tilde{R}}{R + \tilde{R}} \frac{\partial U_1}{\partial \chi} - \frac{U_2}{R + \tilde{R}} \right) + \right.$$

$$\left. + \frac{\partial U_2}{\partial R} \left(\frac{\partial U_2}{\partial R} + \frac{\tilde{R}}{R + \tilde{R}} \frac{\partial U_1}{\partial \chi} - \frac{U_2}{R + \tilde{R}} \right) + 2 \left(\frac{\tilde{R}}{R + \tilde{R}} \frac{\partial U_2}{\partial \chi} + \frac{U_1}{R + \tilde{R}} \right) \right] + \frac{\sigma B^* \tilde{R}^2}{(R + \tilde{R})^2} U_2^2 \quad (12)$$

$$\left[\frac{\partial C}{\partial t} + U_1 \frac{\partial C}{\partial R} + \frac{R U_2}{R + \tilde{R}} \frac{\partial C}{\partial \chi} \right] = D \left[\frac{\partial^2 C}{\partial R^2} + \frac{\tilde{R}}{R + \tilde{R}} \frac{\partial C}{\partial R} + \left(\frac{\tilde{R}}{R + \tilde{R}} \right)^2 \frac{\partial^2 C}{\partial \chi^2} \right] +$$

$$+ \frac{DK_T}{T_m} \left[\frac{\partial^2 T}{\partial R^2} + \frac{\tilde{R}}{R + \tilde{R}} \frac{\partial T}{\partial R} + \left(\frac{\tilde{R}}{R + \tilde{R}} \right)^2 \frac{\partial^2 T}{\partial \chi^2} \right] \quad (13)$$

The boundary conditions associated with eqs. (9)-(13) [14]:

$$U_2 = 0, U_1 = \frac{\partial H_1}{\partial t}, T = T_0, C = C_0 \quad \text{at } R = H_1(\chi, t) \quad (14)$$

$$U_2 = 0, U_1 = \frac{\partial H_2}{\partial t}, T = T_1, C = C_1 \quad \text{at } R = H_2(\chi, t) \quad (15)$$

In order to shift from fixed frame (R, χ) to wave frame (r, x) , we employ the transformations:

$$x = \chi - ct, r = R, p = P, u_1 = U_1, u_2 = U_2 - c, T = T \quad (16)$$

After making use of aforementioned transformations, the governing equations in the wave frame obtained. These equations after defining the dimensionless variables:

$$\bar{x} = \frac{2\pi}{\lambda^*} x, \eta = \frac{r}{a_1}, \bar{u}_1 = \frac{u_1}{c_1}, \bar{u}_2 = \frac{u_2}{c_1}, \bar{p} = \frac{2\pi a_1^2}{\lambda^* \mu c} p, K^* = \frac{a_1^2}{k^*}$$

$$\gamma = \frac{\tilde{R}}{a_1}, \theta = \frac{T - T_1}{T_0 - T_1}, \phi = \frac{C - C_1}{C_0 - C_1}, \delta = \frac{2\pi a_1}{\lambda^*}, F_0 = \frac{CE\rho c_1 a_1}{\mu}$$

and invoking long wavelength and low Reynolds number assumption ($\delta \approx 0, \text{Re} \approx 0$) reduces to:

$$\frac{\partial p}{\partial \eta} = 0 \quad (17)$$

$$-\frac{\partial p}{\partial x} + \frac{1}{\gamma} \left[-\frac{\partial}{\partial \eta} \left\{ (\eta + \gamma) \frac{\partial^2 \psi}{\partial \eta^2} \right\} - \frac{1}{\eta + \gamma} \left(1 - \frac{\partial \psi}{\partial \eta} \right) \right] - \frac{\eta + \gamma}{K^* \gamma} \left(1 - \frac{\partial \psi}{\partial \eta} \right) -$$

$$-\frac{\text{Re}(\eta + \gamma) F_0}{\gamma \sqrt{K^*}} \left(1 - \frac{\partial \psi}{\partial \eta} \right)^2 - \frac{\gamma \text{Ha}^2}{\eta + \gamma} \left(1 - \frac{\partial \psi}{\partial \eta} \right) = 0 \quad (18)$$

$$\frac{\partial^2 \theta}{\partial \eta^2} + \frac{1}{(\eta + \gamma)} \frac{\partial \theta}{\partial \eta} + \text{Br} \left[-\frac{1}{\eta + \gamma} \left(1 - \frac{\partial \psi}{\partial \eta} \right) - \frac{\partial^2 \psi}{\partial \eta^2} \right]^2 + \frac{\text{BrHa}^2 \gamma^2}{(\eta + \gamma)^2} \left(1 - \frac{\partial \psi}{\partial \eta} \right)^2 = 0 \quad (19)$$

$$\left[\frac{\partial^2 \phi}{\partial \eta^2} + \frac{1}{(\gamma + \eta)} \frac{\partial \phi}{\partial \eta} \right] = -\text{SrSc} \left[\frac{\partial^2 \theta}{\partial \eta^2} + \frac{1}{(\gamma + \eta)} \frac{\partial \theta}{\partial \eta} \right] \quad (20)$$

In previous equations Re is the Reynolds number, δ – the wave number, γ – the dimensionless radius of curvature, F_0 – the Forchheimer parameter, and K^* – the dimensionless permeability parameter, respectively. The stream function ψ and velocity components u_1 and u_2 are related:

$$u_1 = \delta \frac{\gamma}{\eta + \gamma} \frac{\partial \psi}{\partial x}, \quad u_2 = -\frac{\partial \psi}{\partial \eta}$$

Elimination of pressure between eqs. (17) and (18):

$$\begin{aligned} \frac{\partial}{\partial \eta} \left(\frac{1}{\gamma} \left\{ -\frac{\partial}{\partial \eta} \left[(\eta + \gamma) \frac{\partial^2 \psi}{\partial \eta^2} \right] - \frac{1}{\eta + \gamma} \left(1 - \frac{\partial \psi}{\partial \eta} \right) \right\} - \frac{\eta + \gamma}{K^* \gamma} \left(1 - \frac{\partial \psi}{\partial \eta} \right) - \right. \\ \left. - \frac{\text{Re}(\eta + \gamma) F_0}{\gamma \sqrt{K^*}} \left(1 - \frac{\partial \psi}{\partial \eta} \right)^2 - \frac{\gamma \text{Ha}^2}{\eta + \gamma} \left(1 - \frac{\partial \psi}{\partial \eta} \right) \right) = 0 \end{aligned} \quad (21)$$

The boundary conditions (14) and (15) transform:

$$\psi = -\frac{q}{2}, \quad \frac{\partial \psi}{\partial \eta} = 1, \quad \theta = 0, \quad \phi = 0, \quad \text{at } \eta = h_1 = 1 + \lambda \sin x \quad (22)$$

$$\psi = \frac{q}{2}, \quad \frac{\partial \psi}{\partial \eta} = 1, \quad \theta = 1, \quad \phi = 1, \quad \text{at } \eta = h_2 = -1 - \lambda' \sin x \quad (23)$$

where $\lambda = a/w$ and $\lambda' = b/w$ are the amplitude ratios. In summary, we have to solve eqs. (19)-(21) subject to boundary conditions (22) and (23).

The physical quantities of interest such as pressure rise per wave length friction, Δp , forces, heat transfer coefficients at both the wall $z_i (i = 1, 2)$ and Sherwood number at both the wall $\text{Sh}_i (i = 1, 2)$ are defined [8, 13]:

$$\Delta p = \int_0^{2\pi} \frac{dp}{dx} dx \quad (24)$$

$$F_u = \int_0^{2\pi} -h_1 \frac{dp}{dx} dx, \quad F_t = \int_0^{2\pi} -h_2 \frac{dp}{dx} dx \quad (25)$$

$$z_i = \frac{\partial h_i}{\partial x} \frac{\partial \theta}{\partial \eta} \Big|_{\eta=h_i}, \quad i = 1, 2 \quad (26)$$

$$\text{Sh} = \frac{\partial h_i}{\partial x} \frac{\partial \phi}{\partial \eta} \Big|_{\eta=h_i}, \quad i = 1, 2. \quad (27)$$

Now, in order to solve eqs. (19)-(21) an implicit finite difference technique is employed for the solution.

Method of solution

In this part, we briefly describe the finite difference scheme used for the solution of eqs. (19)-(21) subject to boundary conditions given in eqs. (22) and (23). In this procedure the

original non-linear boundary value problem is converted into a linear one at the $(m + 1)^{\text{th}}$ iterative step. For this particular problem, the following iterative procedure:

$$\begin{aligned} \frac{\partial^4 \psi^{(m+1)}}{\partial \eta^4} + \frac{\partial^3 \psi^{(m+1)}}{\partial \eta^3} - \left\{ \frac{1}{\eta + \gamma} + \frac{\eta + \gamma}{K^*} + \frac{2 \operatorname{Re}(\eta + \gamma) F_0}{\sqrt{K^*}} \left(1 - \frac{\partial \psi^{(m)}}{\partial \eta} \right) + \frac{\gamma^2 \operatorname{Ha}^2}{\eta + \gamma} \right\} \frac{\partial^2 \psi^{(m+1)}}{\partial \eta^2} \\ - \left\{ -\frac{1}{(\eta + \gamma)^2} + \frac{1}{K^*} + \frac{\operatorname{Re} F_0}{\sqrt{K^*}} \left(\frac{\partial \psi^{(m)}}{\partial \eta} - 2 \right) - \frac{\gamma^2 \operatorname{Ha}^2}{(\eta + \gamma)^2} \right\} \frac{\partial \psi^{(m+1)}}{\partial \eta} - \frac{1}{(\eta + \gamma)^2} + \frac{1}{K^*} + \\ + \frac{\operatorname{Re} F_0}{\sqrt{K^*}} - \frac{\gamma^2 \operatorname{Ha}^2}{(\eta + \gamma)^2} = 0 \end{aligned} \quad (28)$$

$$\frac{\partial^2 \theta^{(m+1)}}{\partial \eta^2} + \frac{1}{\gamma + \eta} \frac{\partial \theta^{(m+1)}}{\partial \eta} = -\operatorname{Br} \left[-\frac{1}{\gamma + \eta} \left(1 - \frac{\partial \psi^{(m)}}{\partial \eta} \right) - \frac{\partial^2 \psi^{(m)}}{\partial \eta^2} \right]^2 - \frac{\operatorname{Br} \operatorname{Ha}^2 \gamma^2}{(\gamma + \eta)^2} \left[1 - \frac{\partial \psi^{(m)}}{\partial \eta} \right]^2 \quad (29)$$

$$\frac{\partial^2 \phi^{(m+1)}}{\partial \eta^2} + \frac{1}{\eta + k} \frac{\partial \phi^{(m+1)}}{\partial \eta} = -\operatorname{SrSc} \left[\frac{\partial^2 \theta^{(m)}}{\partial \eta^2} + \frac{1}{(k + \eta)} \frac{\partial \theta^{(m)}}{\partial \eta} \right] \quad (30)$$

$$\psi^{m+1} = -\frac{q}{2}, \quad \frac{\partial \psi^{m+1}}{\partial \eta} = 1, \quad \theta^{(m+1)} = 0, \quad \phi^{(m+1)} = 0 \quad \text{at } \eta = h_1 \quad (31)$$

$$\psi^{(m+1)} = \frac{q}{2}, \quad \frac{\partial \psi^{(m+1)}}{\partial \eta} = 1, \quad \theta^{(m+1)} = 1, \quad \phi^{(m+1)} = 1 \quad \text{at } \eta = h_2 \quad (32)$$

where the index (m) shows the iterative step.

In the next step, we insert finite difference approximations of $\psi^{(m+1)}$, $\theta^{(m+1)}$, $\phi^{(m+1)}$, and their derivatives into eqs. (28)-(30). In this way, we get a system of linear algebraic equations at each iterative step. These algebraic equations are solved at each cross-section get numerical results of $\psi^{(m+1)}$, $\theta^{(m+1)}$, and $\phi^{(m+1)}$. It is important to note that, suitable initial guesses are required for $\psi^{(m)}$, $\theta^{(m)}$, and $\phi^{(m)}$, at each cross-section start the iterative procedure. For present computation, linear initial guesses (only satisfying the Dirichlet boundary conditions) are used. The iterative procedure at each cross-section is carried out until a convergent solution is reached. The convergent solution is obtained rapidly by method of successive under-relaxation. In this method the values of $\tilde{\psi}^{(m+1)}$, $\tilde{\theta}^{(m+1)}$, and $\tilde{\phi}^{(m+1)}$ at $(m+1)^{\text{th}}$ iterative step are used to define convergent values $\psi^{(m+1)}$, $\theta^{(m+1)}$, and $\phi^{(m+1)}$ at the same step as:

$$\begin{aligned} \psi^{(m+1)} &= \psi^{(m)} + \tau \left[\tilde{\psi}^{(m+1)} - \psi^{(m)} \right] \\ \theta^{(m+1)} &= \theta^{(m)} + \tau \left[\tilde{\theta}^{(m+1)} - \theta^{(m)} \right] \\ \phi^{(m+1)} &= \phi^{(m)} + \tau \left[\tilde{\phi}^{(m+1)} - \phi^{(m)} \right] \end{aligned}$$

where τ is under relaxation parameter usually assumed small. In present computation the iterative procedure is terminated after achieving the values of ψ , θ , and ϕ convergent to 10^{-8} .

Algorithm validation

Before embarking on the physical interpretation of the obtained results it is better to validate our results by comparing them with the existing results in the literature. To this end,

we have prepared figs. 2 and 3. Figure 2 presents a comparison of velocity profile $u(\eta)$ computed using present numerical scheme for $K^* \rightarrow \infty$, $Ha = 0$, $\gamma = 2$, $\lambda = 0.4$, $x = 0$, $\theta = 1$ (solid line) with the velocity profile given in fig. 3 of [5] corresponding to $k = 2$, $\phi = 0.4$, $x = 0$, and $\theta = 1$ (superimposed dots). Clearly, both curves coincide showing an excellent agreement between our results with the existing ones. Figure 3 shows a comparison of temperature profile, $\theta(\eta)$, based on our numerical scheme for $\lambda = 0.4$, $x = 0$, $\gamma = 2$, and $\Theta = 1$ (solid line) with the temperature profile in fig. 4 of [14] corresponding to $\Theta = 1$, $\phi = 0.4$, $x = 0$, $k = 2$ (superimposed dots). Again, an excellent correlation is achieved which clearly testifies validity our numerical results.

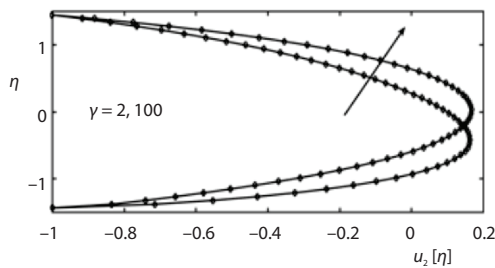


Figure 2. Comparison of present results for velocity (solid line) with the results for velocity reported in [5] (superimposed line)

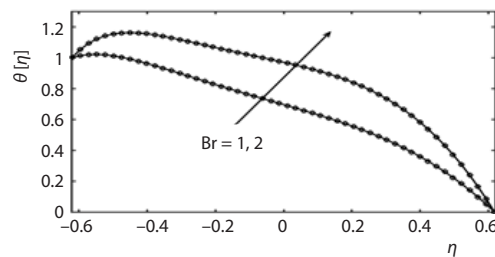


Figure 3. Comparison of present results for temperature (solid line) with the results for temperature reported in [14] (superimposed line)

Computational results and their interpretation

In this section, we interpret the graphical results provided in figs. 4-28 to analyze some significant features of the peristaltic motion such as *flow characteristics*, *pumping characteristics*, *temperature distribution*, *mass concentration*, and *trapping phenomenon* for various values of the parameters curvature parameter, γ , Forchiemmer parameter, F_0 , Brinkman number, Br, and permeability parameter, K^* . The variation of friction forces and heat and mass transfer coefficients at both upper and lower walls is also shown.

The axial velocity distribution for some specific values of Forchiemmer parameter, F_0 , permeability parameter, K^* , Hartmann number, Ha, and curvature parameter, γ , is shown in figs. 4-7, respectively. Figure 4 shows that axial velocity is suppressed with increasing Forchiemmer parameter. With increasing Forchiemmer parameter, the velocity profile becomes asymmetric with maximum appearing below the curve $\eta = 0$. The Forchiemmer parameter is the ratio of solid-liquid interaction of viscous resistance. Larger values of F_0 correspond to the situation when viscous resistance is smaller in comparison resistance due to the solid obstacles. Therefore, the suppression of velocity amplitude observed in fig. 4 for larger values of F_0 is attributed to the increase in resistance due to the solid obstacles. Figure 5 shows the effects of permeability parameter on velocity, u_2 . Smaller values of K^* correspond to weaker porous medium effects while larger values represent the case when resistance due to porous matrix is strong. It is observed that larger values of K^* impede the velocity amplitude and shift the maximum velocity away from the lower wall of the channel towards the central line, $\eta = 0$. Figure 6 demonstrates the effects of applied magnetic field on the flow velocity. Here it is quite obvious that flow velocity exhibits boundary-layer character for larger values of Hartmann number. In fact for large values of Hartmann number, the disturbance in flow velocity is confined in thin layer near both upper and lower walls. The fluid outside the boundary-layer moves with a velocity which varies linearly with radial co-ordinate, η . In contrast, the fluid outside the boundary-layers moves with constant velocity in a straight channel. It is further noted from fig. 6 that the axial velocity

for moderate values of Hartmann number recaptures its symmetric profile. The boundary-layer character exhibited by the flow velocity is due to resistive nature of magnetic force. This resistance due to magnetic force suppresses the flow in the vicinity of the channel center. In order to maintain the prescribed mass flux, the velocity near the boundary walls will rise. The simultaneous occurrence of both these phenomena leads to the function of boundary-layer at the channel walls. Figure 7 depicts the effects of dimensionless radius of curvature, γ , on velocity distribution. For smaller values of γ the velocity is asymmetric about $\eta = 0$ with maximum appearing in the lower half of the channel. The asymmetry in flow velocity is due to the pressure accelerated fluid layers near lower wall of channel due to curvature. With increasing γ , the velocity regains its symmetry about $\eta = 0$. This is expected because for large values of γ channel becomes straight.

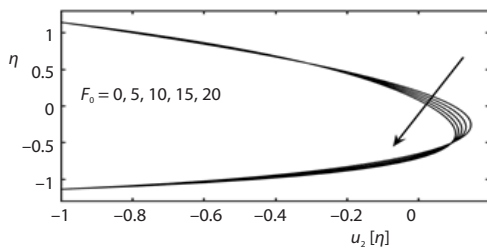


Figure 4. The $u_2(\eta)$ for various values of F_0 with $\gamma = 1.5$, $K^* = 2$, $Ha = 0.5$, $\lambda = 0.4$, and $\Theta = 1.5$

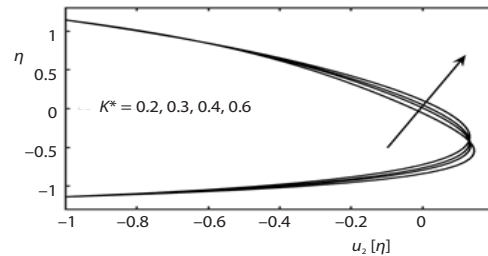


Figure 5. The $u_2(\eta)$ for various values of K^* with $\gamma = 1.5$, $F_0 = 2$, $Ha = 0.5$, $\lambda = 0.4$ and $\Theta = 1.5$

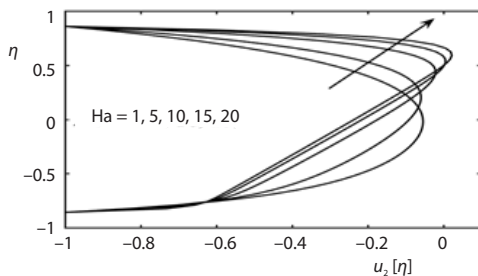


Figure 6. The $u_2(\eta)$ for various values of Ha with $\gamma = 1.5$, $F_0 = 2$, $K^* = 0.2$, $\lambda = 0.4$, and $\Theta = 1.5$

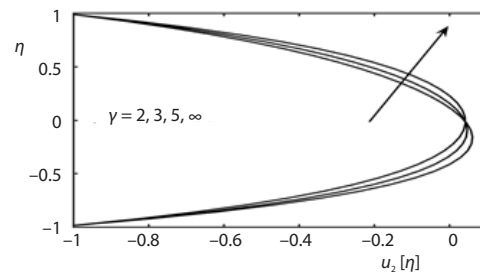


Figure 7. The $u_2(\eta)$ for various values of γ with $K^* = 0.2$, $F_0 = 2$, $Ha = 0.2$, $\lambda = 0.4$, and $\Theta = 1.5$

Figures 8-11 demonstrate the effect of different parameters on pressure rise per wavelength. Figure 8 depicts the effects of Forchheimer parameter on Δp . No peristaltic pumping region can be identified from this figure. The maximum pressure rise against which peristalsis has to work (*i. e.*, Δp corresponding to $\theta = 0$) is zero. This clearly indicate that for suitable choice of involved parameters the resistance offered by pressure gradient to peristaltic flow can be avoided. The profile of pressure rise per wavelength for different values of K^* (permeability parameter) is shown in fig. 9. Here, it is noted that in peristaltic pumping region ($\Theta > 0$, $\Delta p > 0$) Δp increases with decreasing the permeability of the porous medium for a fixed value of prescribed flow rate. Thus, in the present settings the porous medium inside the channel hampers the normal flow of the fluid and peristalsis has to do greater work against the pressure rise to maintain the same flux as in the case of clear medium inside the channel. This eventually reduces the pumping efficiency. Figures 10 and 11 are plotted to see the variation of Δp against dimensionless mean flow rate, Θ , for various values of Hartmann number and γ , respectively. In pumping region ($\Theta > 0$, $\Delta p > 0$) pressure rise per wavelength increases, by increasing Hartmann number.

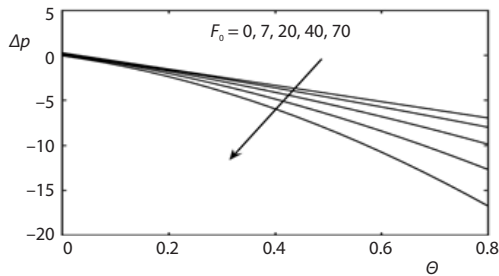


Figure 8. The Δp for various values of F_0 with $\gamma = 2$, $K^* = 2$, $Ha = 0.5$, and $\lambda = 0.4$

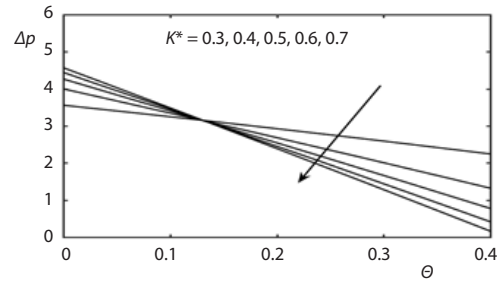


Figure 9. The Δp for various values of K^* with $\gamma = 2$, $F_0 = 2$, $Ha = 0.5$, and $\lambda = 0.4$

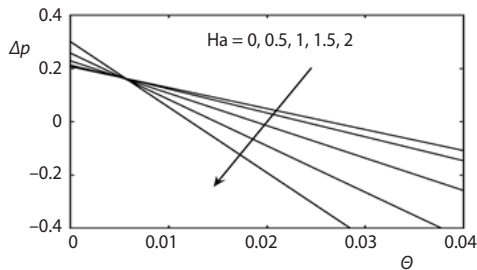


Figure 10. The Δp for various values of Ha with $\gamma = 2$, $K^* = 2$, $F_0 = 2$, and $\lambda = 0.4$

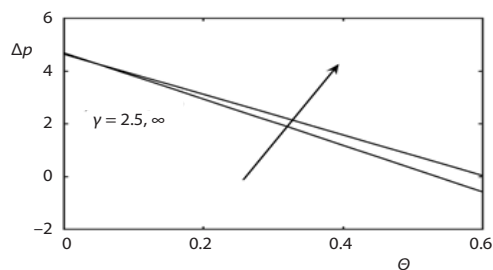


Figure 11. The Δp for various values of γ with $Ha = 0.2$, $K^* = 0.5$, $\gamma = 2$, and $\lambda = 0.4$

The situation is different in free pumping ($\Delta p = 0$) and co-pumping region ($\Theta > 0$, $\Delta p < 0$). Here Δp decreases by increasing Hartmann number. Figure 11 shows that Δp in pumping region decreases in going from curved to straight channel below a certain critical value of Θ . Above this critical value a reverse trend is observed. This reverse trend also prevails in free pumping and co-pumping regions. The friction forces at upper and lower walls denoted by F_u and F_l , respectively, for different values of Forchiemmer parameter, permeability parameter, and Hartmann number are shown in figs. 12-14. It is observed that the behavior of friction forces is opposite to that of pressure rise. Moreover, they resist the flow in the pumping region and magnitude of resistance increases with increasing permeability parameter and Hartmann number. However, the resistance due to friction forces in pumping region decreases with increasing Forchiemmer parameter. Further, resistance at lower wall is greater than at upper wall.

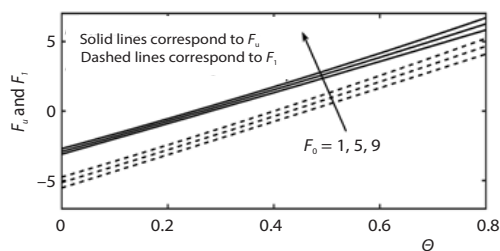


Figure 12. Friction forces at upper and lower walls for various values of F_0 with $Ha = 0.2$, $K^* = 0.5$, $\gamma = 2$, and $\lambda = 0.4$

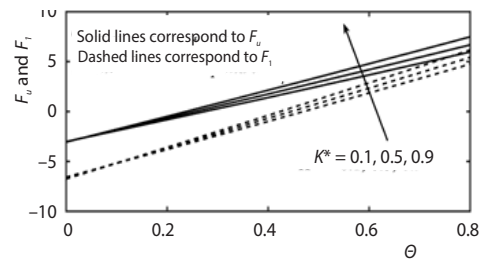


Figure 13. Friction forces at upper and lower walls for various values of K^* with $F_0 = 2$, $\gamma = 2$, and $\lambda = 0.4$

The radial distribution of temperature of the fluid inside the channel for different values of Brinkmann number, permeability parameter, Hartman number, and Forchiemmer parameter is

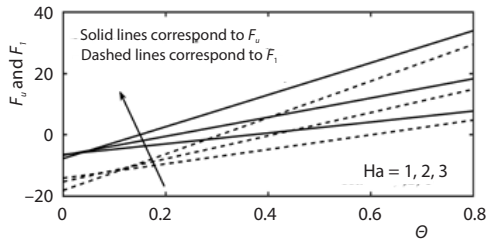


Figure 14. Friction forces at upper and lower walls for various values of Ha with $F_0 = 2$, $\gamma = 2$, and $\lambda = 0.4$

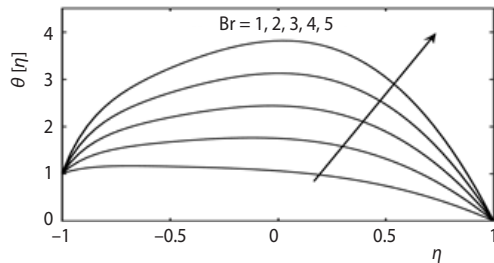


Figure 15. Profile of temperature $\theta(\eta)$ for various values of Br with $F_0 = 2$, $\lambda = 0.4$, $\gamma = 2$, and $\Theta = 1.2$

shown in figs. 15-18. Here it is noted that the effect of Br, K^* , and Ha is to increase the fluid temperature inside the channel while the effect of CE is quite opposite. It is observed that an increase in Forchiemmer parameter impedes the fluid motion only in the vicinity of the channel and velocity over rest of the cross-section is unaffected with change in CE. Due to this reason the heat transfer rate from boundaries to the fluid is reduced and the fluid temperature is decreased inside the channel with increasing Forchiemmer parameter.

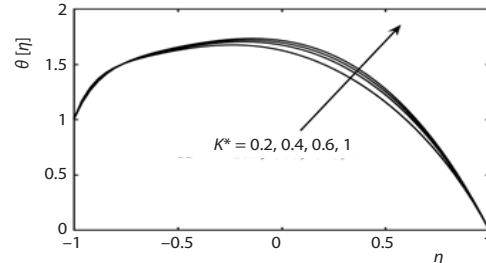


Figure 16. Profile of temperature $\theta(\eta)$ for various values of K^* with $F_0 = 2$, Br = 2, $\lambda = 0.4$, $\gamma = 2$, and $\Theta = 1.2$

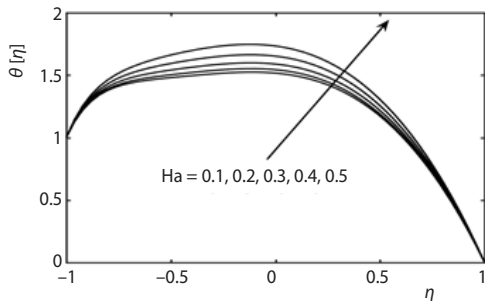


Figure 17. Profile of temperature $\theta(\eta)$ for various values of Ha with $F_0 = 2$, Br = 2, $\lambda = 0.4$, $\gamma = 2$, and $\Theta = 1.2$

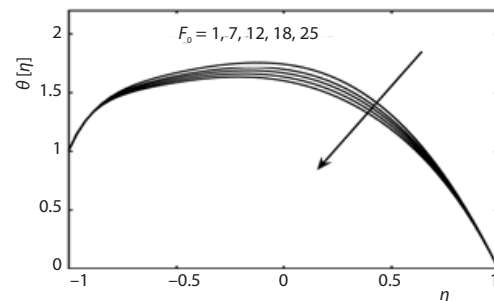


Figure 18. Profile of temperature $\theta(\eta)$ for various values of F_0 with Br = 2, $\lambda = 0.4$, $\gamma = 2$, and $\Theta = 1.2$

The variations of heat transfer coefficient z at both walls for different values of F_0 , Ha, and Br are shown through fig. 19. The profiles of z are clearly oscillating (periodic) due to periodic oscillating nature of the boundary walls. The amplitude of oscillation increases with increasing F_0 , Ha, and Br. The profiles of mass concentration inside the channel with several values of Br, K^* , Ha, and F_0 are shown in figs. 20-23. It is observed that the behavior of mass concentration is similar to behavior of temperature *i. e.* mass concentration inside the channel increases with increasing Br, K^* , and Ha while its magnitude reduces with increasing F_0 . The effects of Forchiemmer parameter, Hartmann number, and Brinkmann number on Sherwood number at both walls are shown through fig. 24. It is observed that Sherwood number also exhibits oscillatory behavior and its amplitude at both walls increases with increasing F_0 and Br. In contrast, the amplitude at lower wall (upper wall) decreases (increasing) with increasing the strength of the applied magnetic field.

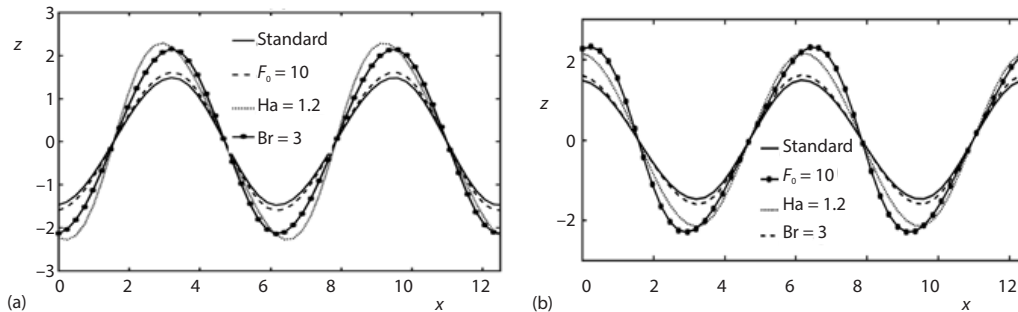


Figure 19. Variation of heat transfer coefficient z at upper; (a) and lower (b) walls for different parameters with $\Theta = 1.5$, $\lambda = 0.4$, and $\gamma = 2$

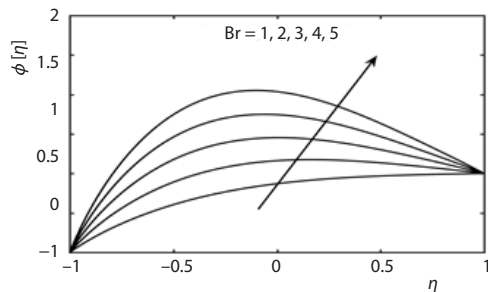


Figure 20. Variation of mass concentration ϕ for Br with $Ha = 1$, $Sr = 0.5$, $Sc = 0.2$, $\lambda = 0.4$, and $\gamma = 2$

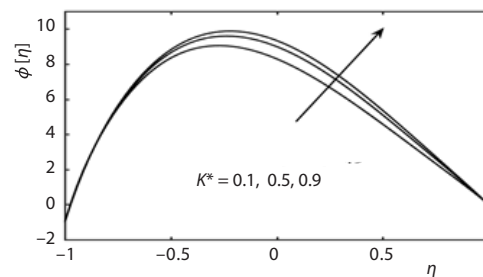


Figure 21. Variation of mass concentration ϕ for K^* with $Br = 2$, $Sr = 0.5$, $Sc = 0.2$, $\lambda = 0.4$, and $\gamma = 2$

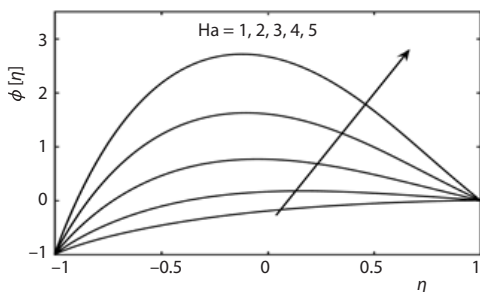


Figure 22. Variation of mass concentration ϕ for Ha with $Br = 2$, $Sr = 0.5$, $Sc = 0.2$, $K^* = 0.5$, $\lambda = 0.4$, and $\gamma = 2$

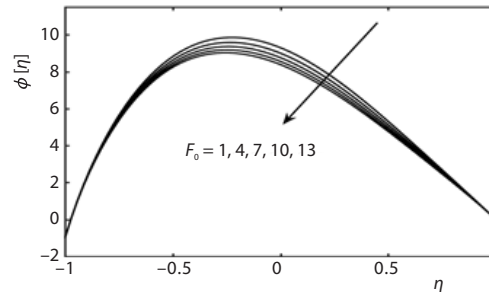


Figure 23. Variation of mass concentration ϕ for F_0 with $Br = 2$, $K^* = 0.5$, $Sr = 1.5$, $Sc = 1.2$, $\lambda = 0.4$, and $\gamma = 2$

The streamline of flow inside the channel for different values of Forchheimer parameter, permeability parameter, Hartman number, and curvature parameter are shown in figs. 25-28. These plots have been prepared to examine the trapping phenomenon in which a volume of the fluid is trapped within closed streamlines. This volume of fluid is often termed as bolus. It is observed that bolus is not significantly affected with an increase in Forchheimer parameter. However, the bolus gets shrinked and center of circulation shift from lower to upper half with increasing K^* . Figure 21 shows the effects of Hartmann number on streamlines. Here it is noted that circulating bolus concentrated in upper half of the channel for $Ha = 0.5$ transforms to the bolus whose center of rotation lies in the lower half of the channel with increasing Hartmann number to 3.5. In the process of transformation the size of the bolus is also reduced. Figure 26 shows that the bolus is asymmetric and concentrated in the upper half of the channel for smaller values of γ

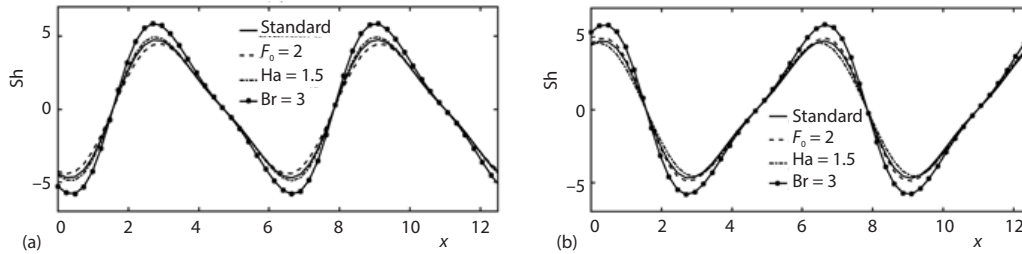


Figure 24. Variation of Sherwood number at upper; (a) and lower (b) walls for different parameters with $\Theta = 1.5, \lambda = 0.4,$ and $\gamma = 2$

i. e. in a curved channel. However, it regains its symmetry when *i. e.* when $\gamma \rightarrow \infty$ channel becomes straight.

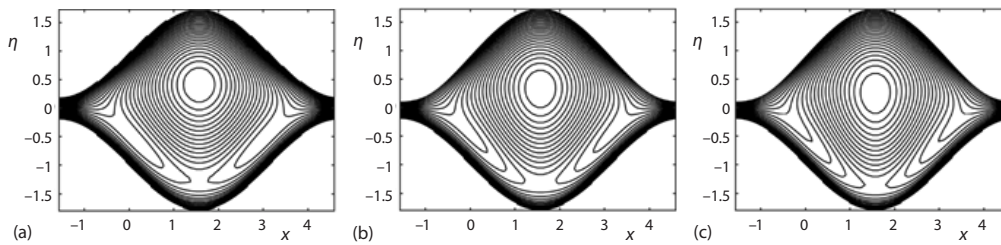


Figure 25. Streamlines in wave frame for (a) $F_0 = 1,$ (b) $F_0 = 5,$ and (c) $F_0 = 10;$ the other parameters chosen are $\gamma = 2, K^* = 2,$ and $\lambda = 0.8$

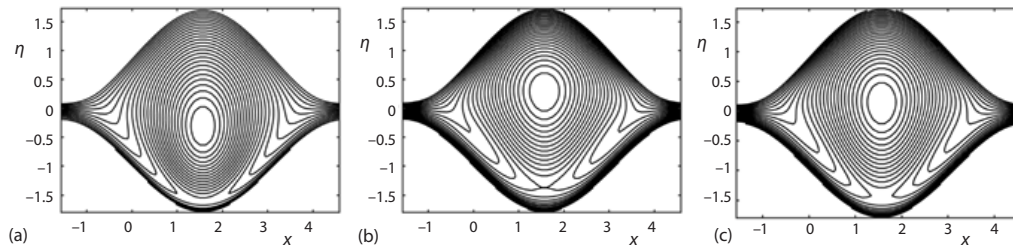


Figure 26. Streamlines in wave frame for (a) $K^* = 0.1,$ (b) $K^* = 0.5,$ and (c) $K^* = 1;$ the other parameters chosen are $F_0 = 1.5, \gamma = 2,$ and $\lambda = 0.8$

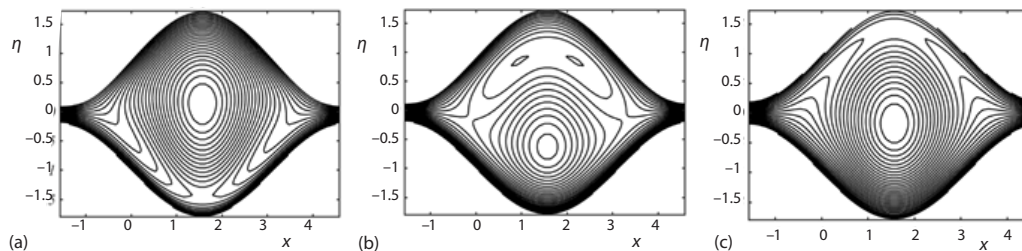


Figure 27. Streamlines in wave frame for (a) $Ha = 0.5,$ (b) $Ha = 2.5,$ and (c) $Ha = 3.5;$ the other parameters chosen are $F_0 = 1.5, \gamma = 2, K^* = 0.5,$ and $\lambda = 0.8$

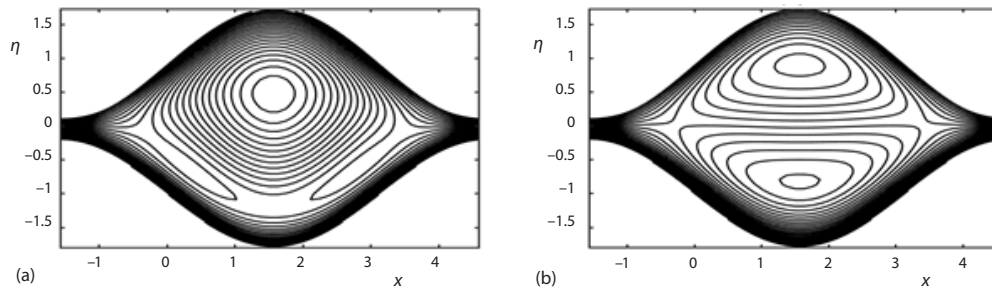


Figure 28. Streamlines in wave frame for (a) $\gamma = 3$ and (b) $\gamma \rightarrow \infty$; the other parameters chosen are $F_0 = 1.5$, $Ha = 0.5$, $K^* = 0.5$, and $\lambda = 0.8$

Conclusions

The flow induced by peristaltic waves inside a curved porous-saturated channel is numerically simulated under long wavelength assumption with Darcy-Forchheimer law and Joule heating effect. The behavior of velocity, pressure, temperature, mass concentration and streamlines is shown through graphs. The key findings of the analysis are:

- The flow velocity diminishes with increasing K^* and Hartmann number.
- Pressure rise per wavelength increases with increasing K^* and Hartmann number. In contrast, Δp is nearly independent of F_0 in pumping region. In fact it is possible to choose the plausible of F_0 for which Δp corresponding to $\Theta = 0$.
- The radial distribution of temperature inside the channel follow increasing trend with increasing Brinkmann number, K^* , and Hartmann number, while it decreases with increasing F_0 .
- The size of circulating bolus of fluid reduces with increasing K^* and Hartmann number.
- The bolus size is nearly unaffected with increasing F_0 .
- Greater peristaltic mixing is achieved with increasing Hartmann number and curvature of the channel.
- The symmetry in velocity and streamlines pattern is observed when $\gamma \rightarrow \infty$.

Nomenclature

B^* – magnetic field, [Wb m^{-2}]
 C – mass concentration, [kg]
 c – wave speed, [ms^{-1}]
 D – coefficient of mass diffusivity, [m^2s^{-1}]
 k^* – thermal conductivity, [$\text{W m}^{-1}\text{K}^{-1}$]
 T – temperature, [K]
 T_m – mean fluid temperature, [K]
 T_0 – temperature at lower wall, [K]
 T_1 – temperature at lower wall, [K]
 u_1, u_2 – velocity component, [ms^{-1}]

Greek symbols

γ – dimensionless radius of curvature, [m]
 δ – wave number, [m^{-1}]
 λ, λ' – amplitude ratio, [m]
 μ – viscosity parameter, [$\text{kg m}^{-1}\text{s}^{-1}$]
 ρ – density, [kg m^{-3}]
 σ – Stefan-Boltzman constant, [$\text{W m}^{-2}\text{K}^{-4}$]
 τ – Cauchy stress tensor, [$\text{kg m}^{-1}\text{s}^{-2}$]
 Φ – dissipation function, [$\text{kg m}^{-1}\text{s}^{-3}$]

Reference

- [1] Shapiro, A. H., et al., Peristaltic Pumping with Long Wavelength at Low Reynolds Number, *Journal Fluid Mech.*, 37 (1969), 4, pp. 799-825
- [2] Fung, Y. C., Yih, C. S., Peristaltic Transport, *Trans. ASME J. Appl. Mech.*, 35 (1968), 4, pp. 669-675
- [3] Raju, K. K., Devanathan, R., Peristaltic Motion of Non-Newtonian Fluid, *Acta*, 11 (1972), 2, pp. 170-178
- [4] Siddiqui, A. M., Schwarz, W. H., Peristaltic Flow of Second Order Fluid in Tubes, *Journal Non-Newtonian Fluid Mech.*, 30 (1994), July, pp. 257-284
- [5] Ali, N., et al., Non-Newtonian Fluid-Flow Induced by Peristaltic Waves in a Curved Channel, *European Journal of Mechanics-B/Fluids*, 29 (2010), 5, pp. 384-397

- [6] Bohme, G., Muller, A., Analysis of Non-Newtonian Effects in Peristaltic Pumping, *Journal of Non-Newtonian Fluid Mech.*, 201 (2013), Nov., pp. 107-119
- [7] Kalantari, A., et al., Peristaltic Flow of Non-Newtonian Fluids through Curved Channels: A Numerical Study, *Ann. Trans. Nordic Rheol. Soc.*, 21 (2013), Jan., pp. 163-170
- [8] Kwang-Hua, C. W., Stokes Slip Flow between Corrugated Walls, *ZAMP*, 47 (1996), 4, pp. 591-598
- [9] El-Shehawy, E. F., et al., Slip Effects on the Peristaltic Flow of a Non-Newtonian Maxwellian Fluid, *Acta Mech.*, 186 (2006), 1-4, pp. 141-159
- [10] Ali, N., et al., Slip Effects on the Peristaltic Flow of a Third Grade Fluid in a Circular Cylindrical Tube, *Journal App. Mech.*, 76 (2009), 1, pp. 1-10
- [11] Bandopadhyay, A., Tripathi, D. and Chakraborty, S., Electroosmosis-modulated peristaltic transport in micro-fluidic channel, *Phy. Fluids*, 28 (2016), May, 052002
- [12] Vajravelu, K., et al., Peristaltic Flow and Heat Transfer in a Vertical Porous Annulus with Long Wave-length Approximation, *Int. J. Non-linear Mech.*, 42 (2008), 5, pp. 754-759
- [13] Mekheimer, Kh. S., Abd Elmaboud, Y., The Influence of Heat Transfer and Magnetic Field on Peristaltic Transport of a Newtonian Fluid in a Vertical Annulus: Application of Endoscope, *Phy. Letters A*, 372 (2008), 10, pp. 1657-1665
- [14] Ali, N., et al., Heat Transfer Analysis of Peristaltic Flow in a Curved Channel, *Int. J. Heat Mass Transfer*, 53 (2010), 15-16, pp. 3319-3325
- [15] Tripathi, D., et al., Mathematical Modelling of Heat Transfer Effects on Swallowing Dynamics of Visco-elastic Flood Bolus through the Human Esophagus, *Int. J. Thermal Sci.*, 70 (2013), Aug., pp. 41-53
- [16] Eldabe, N. T. M., et al., Mixed Convective Heat and Mass Transfer in a Non-Newtonian Fluid at a Peristaltic Surface with Temperature Dependent Viscosity, *Arch. Appl. Mech.*, 78 (2008), 8, pp. 599-624
- [17] Srinivas, S., Kothandapani, M., The Influence of Heat and Mass Transfer on MHD Peristaltic Flow through a Porous Space with Compliant Walls, *Appl. Math. Comput.*, 213 (2009), 1, pp. 197-208
- [18] Hayat, T., et al., Effect of Wall Properties on the Peristaltic Flow of a Third Grade Fluid in a Curved Channel with Heat and Mass Transfer, *Int. J. Heat Mass Transfer*, 54 (2011), 23-24, pp. 5126-5136
- [19] Srinivas, S., et al., Mixed Convective Heat and Mass Transfer in an Asymmetric Channel with Peristalsis, *Commun. Non-linear Sci. Numer. Simul.*, 16 (2011), 4, pp. 1845-1862
- [20] Ahmed, R., et al., Heat and Mass Transfer Effects on the Peristaltic Flow of Sisko Fluid in a Curved Channel, *Thermal Science*, 21 (2017), 1, pp. 331-345
- [21] Aarts, A. C. T., Ooms, G., Net Flow of Compressible Viscous Liquids Induced by Travelling Waves in Porous Media, *Journal Eng. Math.*, 34 (1998), 4, pp. 435-450
- [22] Haroun, M. H., Effect of Deborah Number and Phase Difference on Peristaltic Transport of a Third-Order Fluid in an Asymmetric Channel, *Commun. Non-linear Sci. Numer. Simul.*, 12 (2007), 8, pp. 1464-1480
- [23] Hayat, T., et al., The MHD Peristaltic Motion of Johnson-Segalman Fluid in a Channel with Compliant Walls, *Phy. Letter A*, 372 (2008), 30, pp. 5026-5036
- [24] Ali, N., et al., Peristaltic Flow of a Maxwell Fluid in a Channel with Compliant Walls, *Chaos Solitons and Fractals*, 39 (2009), 1, pp. 407-416
- [25] Mekheimer, Kh. S., Abd-El-Wahab, A. N., Net Annulus Flow of a Compressible Viscous Liquid with Peristalsis, *Journal Aero. Eng.*, 25 (2012), 4, pp. 660-669
- [26] Abbasi, A., et al., An Analysis of Peristaltic Motion of Compressible Convected Maxwell Fluid, *AIP Adv.*, 6 (2016), 1, 015119
- [27] Brinkman, H. C., A Calculation of the Viscous Force Exerted by Flowing Fluid on a Dense Swarm of Particles, *Appl. Sci. Research*, 1 (1949), Dec., pp. 27-34
- [28] El-Shehawy, E. F., Peristaltic Transport in an Asymmetric Channel through a Porous Medium, *Appl. Math. Comp.*, 182 (2006), 1, pp. 140-150
- [29] Mekheimer, Kh. S., Non-Linear Peristaltic Transport through a Porous Medium in an Inclined Planar Channel, *Journal Porous Media*, 6 (2003), 3, pp. 189-202
- [30] Kothandapani, M., Srinivas, S., On the Influence of Wall Properties in the MHD Peristaltic Transport with Heat Transfer and Porous Medium, *Phy. Letters A*, 372 (2008), 25, pp. 4586-4591
- [31] Hayat, T., et al., Effect of Heat Transfer on Peristaltic Flow of an Electrically Conducting Fluid in a Porous Space, *Appl. Math. Mod.*, 33 (2009), 4, pp. 1862-1873
- [32] Wang, Y., et al., Magneto Hydrodynamic Peristaltic Motion of a Sisko Fluid in a Symmetric or Asymmetric Channel, *Phy. A*, 387 (2008), 2-3, pp. 347-362
- [33] Hayat, T., Hina, S., The Influence of Wall Properties on the MHD Peristaltic Flow of a Maxwell Fluid with Heat and Mass Transfer, Non-Linear Analysis, *Real World Appl.*, 11 (2010), 4, pp. 3155-3169

- [34] Tripathi, D., Beg, O. A., A Study of Unsteady Physiological Magneto-Fluid-Flow and Heat Transfer through a Finite Length Channel by Peristaltic Pumping, *Proceedings of the Institution of Mechanical Engineers – Part H: Journal Eng. Med.*, 226 (2012), 8, pp. 631-644
- [35] Reddy, M. G., Heat and Mass Transfer on Magnetohydrodynamic Peristaltic Flow in a Porous Medium with Partial Slip, *Alexandria Engineering Journal*, 55 (2016), 2, pp. 1225-1234
- [36] Reddy, M. G., Velocity and Thermal Slip Effects on MHD Third Order Blood Flow in an Irregular Channel through a Porous Medium with Homogenous/Heterogeneous Reactions, *Non-Linear Engineering*, 6 (2017), 3, pp. 167-179
- [37] Reddy, M. G., Makinde, O. D., Magnetohydrodynamic Peristaltic Transport of Jeffrey Nanofluid in an Asymmetric Channel, *Journal Mol. Liq.*, 223 (2016), Nov., pp. 1242-1248
- [38] Reddy, M. G., et al., Heat Transfer on MHD Peristaltic Rotating Flow of a Jeffrey Fluid in an Asymmetric Channel, *Int. J. Appl. Comput. Math.*, 3 (2017), 4, pp. 3201-3227
- [39] Reddy, M. G., et al., Hydromagnetic Peristaltic Motion of a Reacting and Radiating Couple Stress fluid in an Inclined Asymmetric Channel Filled with a Porous Medium, *Alexandria Engineering Journal*, 55 (2016), 2, pp. 1841-1853
- [40] Reddy, M. G., et al., Cross Diffusion Impacts on Hydromagnetic Radiative Peristaltic Carreau-Casson Nanofluids Flow in an Irregular Channel, *Defect and Diffusion Forum*, 377 (2017), Sept., pp. 62-83
- [41] Makinde, O. D., et al., Effects of Thermal Radiation on MHD Peristaltic Motion of Walter-B Fluid with Heat Source and Slip Conditions, *Journal Appl. Flu. Mech.*, 10 (2017), 4, pp. 1105-1112
- [42] Hayat, T., et al., Slip and Joule Heating Effects in Mixed Convection Peristaltic Transport of Nanofluid with Soret and Dufour Effects, *Journal Mol. Liq.*, 194 (2014), June, pp. 93-99
- [43] Hayat, T., et al., Simultaneous Effects of Slip and Wall Properties on MHD Peristaltic Motion of Nanofluid with Joule Heating, *Journal Magn. Mater.*, 395 (2015), Dec., pp. 48-58
- [44] Reddy, M. G., Reddy, K. V., Influence of Joule Heating on MHD Peristaltic Flow of a Nanofluid with Compliant Walls, *Proc. Eng.*, 127 (2015), Dec., pp. 1002-1009